

INTRODUCING THE NEXT-GENERATION ADVANCED BASELINE IMAGER ON GOES-R

BY TIMOTHY J. SCHMIT, MATHEW M. GUNSHOR, W. PAUL MENZEL, JAMES J. GURKA, JUN LI,
AND A. SCOTT BACHMEIER

The ABI will begin a new era in U.S. environmental remote sensing with more spectral bands, faster imaging, and higher spatial resolution than the current imager.

The Advanced Baseline Imager (ABI) is being developed as the future imager on the Geostationary Operational Environmental Satellite (GOES) series, slated to be launched in approximately 2012 with GOES-R (Gurka and Dittberner 2001). Similar to the current GOES imager, ABI will be used for a wide range of qualitative and quantitative weather, oceanographic, climate, and environmental applications. ABI will offer more spectral bands, higher spatial resolution, and faster imaging than the current GOES imager. ABI spatial resolution will be

nominally 2 km for the infrared bands and 0.5 km for the $0.64\text{-}\mu\text{m}$ visible band. While the instrument will allow a flexible scanning scenario, two basic modes are envisioned. One mode is that every 15 min ABI will scan the full disk (FD), plus continental United States (CONUS) 3 times, plus a selectable $1000\text{ km} \times 1000\text{ km}$ area every 30 s. The second mode is that the ABI can be programmed to scan the FD iteratively. The FD image can be acquired in approximately 5 min. Given that the current GOES imager takes approximately 25 min for a FD, this implies there will be a fivefold increase in the coverage rate.

ABI has 16 spectral bands; five are similar to the $0.6\text{-}, 4\text{-}, 11\text{-},$ and $12\text{-}\mu\text{m}$ windows and the $6.5\text{-}\mu\text{m}$ water vapor band on the current GOES-8/-9/-10/-11 imagers (Menzel and Purdom 1994; Ellrod et al. 1998), and another is similar to the $13.3\text{ }\mu\text{m}$ on the GOES-12/-N/-O/-P imagers and the GOES-8/-P sounders (Hillger et al. 2003; Schmit et al. 2001, 2002). Additional bands on ABI are $0.47\text{ }\mu\text{m}$ for aerosol detection and visibility estimation; $0.865\text{ }\mu\text{m}$ for aerosol detection and estimation of vegetation health; $1.378\text{ }\mu\text{m}$ to detect very thin cirrus clouds; $1.6\text{ }\mu\text{m}$ for snow/cloud discrimination; $2.25\text{ }\mu\text{m}$ for aerosol and cloud particle size estimation, vegetation, cloud properties/screening, hot-spot detection, moisture

AFFILIATIONS: SCHMIT—NOAA/NESDIS, Office of Research and Applications, Advanced Satellite Products Team, Madison, Wisconsin; GUNSHOR, LI, AND BACHMEIER—Cooperative Institute for Meteorological Satellite Studies, University of Wisconsin—Madison, Madison, Wisconsin; MENZEL—NOAA/NESDIS, Office of Research and Applications, Madison, Wisconsin; AND GURKA—NOAA/NESDIS, Office of Systems Development, Silver Spring, Maryland

CORRESPONDING AUTHOR: Timothy J. Schmit, 1225 West Dayton St., Madison, WI 53706
E-mail: Tim.J.Schmit@noaa.gov
DOI:10.1175/BAMS-86-8-1079

In final form 14 March 2005
©2005 American Meteorological Society

determination, and snow detection; 7.0 and 7.34 μm for midtropospheric water vapor detection and tracking and upper-level sulfur dioxide (SO_2) detection; 8.5 μm for detection of volcanic dust clouds containing sulfuric acid aerosols and estimation of cloud phase; 9.6 μm for monitoring atmospheric total column ozone and upper-level dynamics (Steinbrecht et al. 1998); and 10.35 μm for deriving low-level moisture and cloud particle size. Each of these bands is often used in conjunction with other bands in a multiple-spectral approach for product generation.

There will also be improvements in radiometric performance, image navigation, and registration. Even with smaller detector sizes, the specified signal-to-noise ratio will be better on the ABI than on today's imager. Image navigation specifications call for at least a twofold improvement to 2 km.

A cost-benefit analysis study, undertaken by Mitre Corporation, surveyed a number of areas where economic benefits can be realized. The "total annual marginal benefits showed a combined annual marginal economic benefits from ABI and Hyperspectral Environmental Suite (HES) to be approximately \$1.47B annually (2003 dollars) and a discounted (present value) sum-of-direct benefits of approximately \$7B across a 15-year effective benefit life cycle."

While ABI represents an exciting expansion in geostationary remote sensing capabilities, it will not be operating alone. Where appropriate, ABI will be used in concert with the GOES-R high spectral resolution sounder and, to a lesser extent, the coastal-waters observations, on the GOES HES. The high spatial resolution ABI data will enable detection of subpixel clouds in the HES infrared measurements (Li et al. 2004a), important for improved HES soundings, and the high spectral resolution HES measurements will offer improved surface emissivity estimates needed for ABI skin temperatures and cloud heights. Every product from the current GOES imager will be improved with data from ABI (and HES), and a host of new products will be possible. The improved products will include hurricane intensities, land and sea temperatures, cloud-top heights/temperatures, identification of fires and hot spots, aerosol and smoke detection, insolation, precipitation, and fog. In addition, ABI will be able to detect upper-level SO_2 clouds (given a sufficient density and spatial extent), monitor plant health on a diurnal time scale, and infer cloud-top phase and particle size information.

The enhanced utility of the spectral bands on the GOES-R ABI are being studied in two ways. One way is to use forward model calculations for various atmo-

spheres; the resulting weighting functions and brightness temperatures (BTs) are compared with similar bands on current instruments. Another way is to use existing satellite data; broadband imagers such as the Moderate Resolution Imaging Spectroradiometer (MODIS; King et al. 1992) are resampled to ABI spatial resolutions or high spectral resolution data from the Atmospheric Infrared Sounder (AIRS; Aumann et al. 2003), the National Polar-orbiting Operational Environmental Satellite System (NPOESS) Atmospheric Sounder Testbed-Interferometer (NAST-I; Smith et al. 1999), or Airborne Visible Infrared Imaging Spectrometer (AVIRIS; Vane 1987) which are convolved with simulated ABI Spectral Response Functions (SRF). Both ways are used in this paper to demonstrate future ABI capabilities.

The spectral locations for the six visible/near-infrared bands proposed for ABI are shown in Fig. 1, along with spectral reflectance plots for snow and vegetation; the spectral plots are from the Advanced Spaceborne Thermal Emission and Reflection Radiometer (ASTER) library (see online at <http://speclib.jpl.nasa.gov/>). The additional spectral coverage and spatial resolution over the current imager will allow for the generation of more products, refinement of existing products, and detection of features not previously observed by GOES. These visible/near-infrared bands will enable or improve detection of haze, clouds, surface vegetation, cirrus, snow cover, and aerosol particle sizes. Vegetation estimates can be obtained by comparing the two bands on either side of the 0.72- μm vegetation reflectance transition region, while snow can be determined by comparing

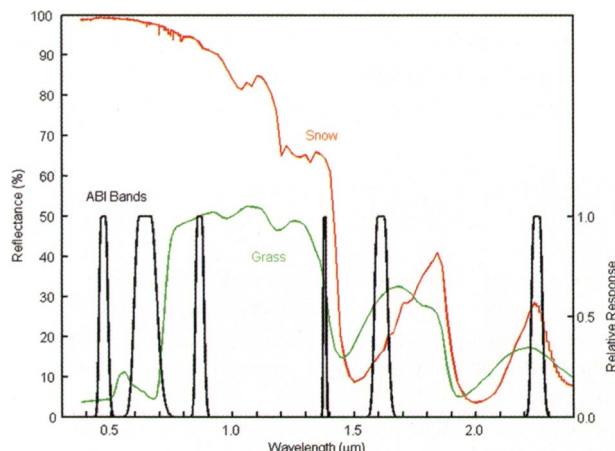


FIG. 1. The spectral coverage of the six visible/near-infrared bands along with spectral plots of reflectance from grass (green curve) and snow (red curve). The current GOES imager has only one visible band centered near 0.65 μm .

two visible bands on either side of the 1.4- μm snow reflectance transition region. Figure 2 shows the spectral locations for the 10 infrared bands proposed for ABI. The spectral coverage of ABI is markedly improved over that of the GOES-8/-9/-10/-11 and the GOES-12/-N/-O/-P imagers. Weighting functions, shown in Fig. 3 for a standard atmosphere at satellite zenith angle of 40°, show that the peak of the ozone-sensitive band is farthest aloft, followed by the three water vapor-weighting functions, and then the CO₂-sensitive band, and, finally, the various surface-viewing bands. These weighting functions display the vertical distribution of upwelling radiance sensed by the ABI infrared (IR) bands. Simulated ABI SRFs were used in a fast radiative transfer model—the Pressure-layer Fast Algorithm for Atmospheric Transmittance (PFAAST; Hannon et al. 1996)—to calculate these weighting functions.

A discussion of the heritage of each spectral band is given in section 2. Section 3 briefly describes each of the bands on the ABI. Some products that are possible with the GOES ABI are summarized in section 4. Finally, a summary is presented in section 5.

HERITAGE OF ABI BANDS. Each ABI band has been chosen to better meet user requirements by building upon experience with satellite and aircraft instruments, and possible synergy with spectral measurements from advanced high spectral resolution instruments. Selection of the ABI bands draws upon the heritage of existing GOES bands (on the GOES-8/-9/-10/-11 and GOES-12/-N/-O/-P imagers and the current GOES sounders), complementary relationship with bands on other operational satellites such as *Meteosat-8*, research satellites such as MODIS, and experience with aircraft test beds such as MODIS Airborne Simulator (MAS). With improved spectral and spatial resolution and higher radiometric accuracy over the current imager, these bands will support weather nowcasting, numerical weather prediction, oceanography, hydrology, land surface, natural hazards, and climate applications [the National Oceanic and Atmospheric Administration/National Environmental Satellite, Data, and

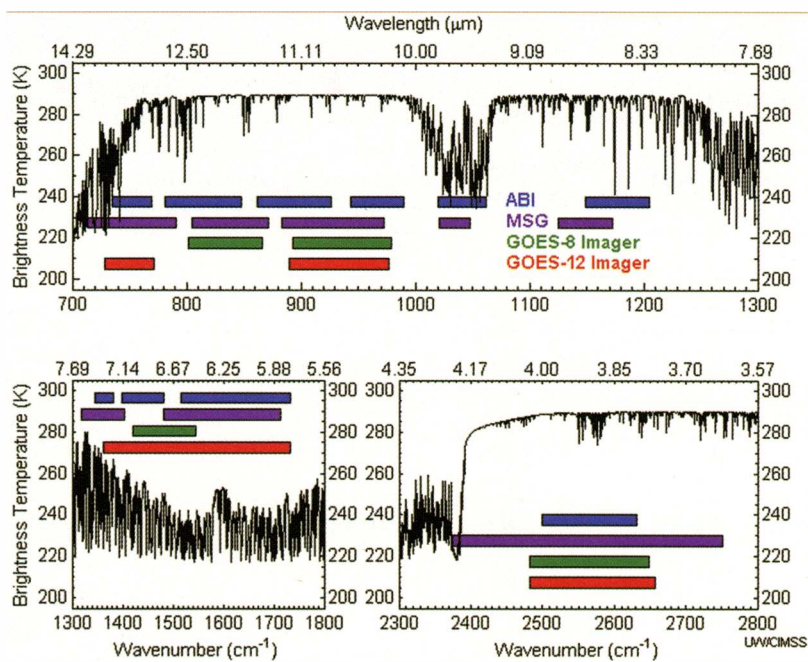


FIG. 2. Spectral coverage of 10 ABI bands in the infrared region superimposed on a calculation of Earth-emitted spectral brightness temperatures for the U.S. Standard Atmosphere, 1976. The spectral coverage of the GOES-8 and -12 imagers, along with that of the Meteosat Second Generation (MSG, now referred to as Meteosat-8) are also shown.

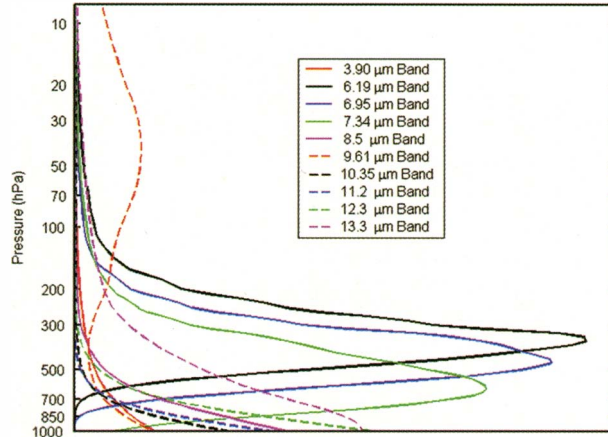


FIG. 3. The ABI-weighting functions are plotted for the U.S. Standard Atmosphere, 1976, at a satellite zenith angle of 40°. The weighting functions were calculated using simulated spectral response functions based on proposed ABI bandwidths.

Information Service (NOAA/NESDIS 2001)]. The primary heritage instrument for each ABI band is summarized in Table 1.

The 0.47- μm band is based on experience with a similar MODIS band. This band has flown on a number of other satellites, including the Sea-viewing Wide Field of view Sensor (SeaWiFS) and is planned for the

TABLE I. Summary of the wavelengths, resolution, and sample use and heritage instrument(s) of the ABI bands. The minimum and maximum wavelength range represent the full width at half maximum (FWHM or 50%) points. [The Instantaneous Geometric Field Of View (IGFOV).]

Future GOES imager (ABI) band	Wavelength range (μm)	Central wavelength (μm)	Nominal subsatellite IGFOV (km)	Sample use	Heritage instrument(s)
1	0.45–0.49	0.47	1	Daytime aerosol over land, coastal water mapping	MODIS
2	0.59–0.69	0.64	0.5	Daytime clouds fog, insulation, winds	Current GOES imager/sounder
3	0.846–0.885	0.865	1	Daytime vegetation/burn scar and aerosol over water, winds	VIIRS, spectrally modified AVHRR
4	1.371–1.386	1.378	2	Daytime cirrus cloud	VIIRS, MODIS
5	1.58–1.64	1.61	1	Daytime cloud-top phase and particle size, snow	VIIRS, spectrally modified AVHRR
6	2.225–2.275	2.25	2	Daytime land/cloud properties, particle size, vegetation, snow	VIIRS, similar to MODIS
7	3.80–4.00	3.90	2	Surface and cloud, fog at night, fire, winds	Current GOES imager
8	5.77–6.6	6.19	2	High-level atmospheric water vapor, winds, rainfall	Current GOES imager
9	6.75–7.15	6.95	2	Midlevel atmospheric water vapor, winds, rainfall	Current GOES sounder
10	7.24–7.44	7.34	2	Lower-level water vapor, winds, and SO_2	Spectrally modified current GOES sounder
11	8.3–8.7	8.5	2	Total water for stability, cloud phase, dust, SO_2 , rainfall	MAS
12	9.42–9.8	9.61	2	Total ozone, turbulence, and winds	Spectrally modified current sounder
13	10.1–10.6	10.35	2	Surface and cloud	MAS
14	10.8–11.6	11.2	2	Imagery, SST, clouds, rainfall	Current GOES sounder
15	11.8–12.8	12.3	2	Total water, ash, and SST	Current GOES sounder
16	13.0–13.6	13.3	2	Air temperature, cloud heights and amounts	Current GOES sounder/GOES-12+ imager

Visible/Infrared Imager and Radiometer Suite (VIIRS) instrument. Also, the *Applications Technology Satellite* (ATS)-3, launched in 1967, provided the first color image of the entire Earth via a multicolor spin scan cloud camera that included this “blue” band (Suomi and Parent 1968). The 0.64- μm band continues the current GOES imager and sounder measurements; a visible band in this spectral range has flown on geostationary imagers since 1966 with ATS-1.

The 0.865- μm band provides geostationary measurements introduced on polar-orbiting Advanced Very High Resolution Radiometer (AVHRR); the ABI band has been spectrally narrowed to minimize influence of a water vapor absorption feature near 0.80 μm , thus, mitigating the effect of atmospheric changes on surface products (M. Griffin 2001, personal communication; Sieglaff and Schmit 2003). The 1.378- μm band has been chosen from experience of MODIS

TABLE 2. Summary of the bands on the current GOES imagers from Hillger et al. (2003). The minimum and maximum wavelength range represent the full width at half maximum (FWHM or 50%) points.

Current GOES imager band	Approximate wavelength range (μm)	Central wavelength (μm)	Nominal subsatellite IGFOV (km)	Sample use
1	0.53–0.75	0.65	1	Cloud cover and surface features during the day
2	3.8–4.0	3.9	4	Low cloud/fog and fire detection
3	6.5–7.0 5.8–7.3	6.7 (GOES-8/-11) 6.5 (GOES-12+)	8 4	Upper-level water vapor
4	10.2–11.2	10.7	4	Surface or cloud-top temperature
5	11.5–12.5	12.0 (GOES-8/-11)	4	Surface or cloud-top temperature and low-level water vapor
6	12.9–13.7	13.3 (GOES-12/-N) 13.3 (GOES-O/-P)	8 4	CO_2 band: Cloud detection

with daytime cirrus clouds and its use within the MODIS cloud mask. The 1.6- μm band has heritage from AVHRR, but has been narrowed (similar to the spectral width of the corresponding MODIS band) to give a less ambiguous cloud-phase determination. The 2.25- μm band is based on experience with the 2.1- μm band on MODIS, but has been shifted spectrally for a better cloud particle size determination (King et al. 2003).

The 3.9- μm band continues current GOES imager measurements. Geostationary applications with this spectral band were first possible with the Visible and Infrared Spin-Scan Radiometer (VISSR) Atmospheric Sounder (VAS) in 1981; the 3.9- μm band was introduced with AVHRR. The 6.19- μm band is based on the current GOES imager and *Meteosat-8*. *Meteosat-8*, the new generation Meteosat (launched in 2002), has 12 bands, including a number of the infrared bands selected for ABI (Schmetz et al. 1998, 2002; Woick et al. 1997). The 6.95- μm is similar to bands on the current GOES sounder and *Meteosat-8*. The 7.34- μm band is based on the current GOES sounder and a similar MODIS band, although this band has been spectrally shifted to better detect upper-level SO_2 . The 8.5- μm band is derived from experience with MODIS for products such as cloud phase, dust detection, and upper-level SO_2 concentration. *Meteosat-8* also carries a similar channel (8.7 μm). The 9.6- μm band was spectrally widened with respect to traditional ozone-sensitive infrared bands on the current GOES sounder to minimize the sensitivity to rapidly changing brightness temperatures. The

10.35- μm band is based on experience with the MAS including cloud-top microphysics and surface properties. The longwave infrared window (11.2 μm) band is similar to many bands on past and existing instruments. The 12.3- μm band, the long wavelength part of the “split window,” is similar to bands on both the GOES-8/-9/-10/-11 imagers and the current sounders. The 13.3- μm band continues measurements from the current sounders and GOES-12/-N/-O/-P imager.

BANDS PROPOSED FOR ABI. The spectral bands proposed for the ABI are summarized in Table 1; approximate spectral widths, central wavelength, and approximate subsatellite point resolutions are indicated. Table 2 gives complementary information about the current GOES imager spectral bands. The current imager oversamples in the east–west by a factor of 1.75 (Menzel and Purdom 1994). The calibrated, navigated ABI data will not be oversampled, but will be remapped to 2-km spatial resolution.

Visible bands. The 0.47- μm band on ABI is intended to provide data throughout the day at mesoscale resolution—a geostationary complement to the polar-orbiting measurements. This band is well established on MODIS in low-Earth orbit on the National Aeronautics and Space Administration’s (NASA’s) *Terra* and *Aqua* platforms. The geostationary 0.47- μm band will provide nearly continuous daytime observations of clouds, dust, haze, and smoke. Measurements of aerosol optical depths (AOD) will help air quality monitoring and forecasting. The geostationary

satellite perspective enables tracking aerosol transport (Kittaka et al. 2004). This blue band ($0.47\text{ }\mu\text{m}$), combined with a green band (which will need to be simulated from other bands and/or sensors) and a red band ($0.64\text{ }\mu\text{m}$), can provide “simulated color” imagery of the Earth, ocean, and atmospheric system. Measurements in the blue band will provide estimates of slant-range visibility that are valuable for aviation applications; shorter wavelengths (blue) are scattered more in haze and air particles than the longer wavelengths (red). The $0.47\text{-}\mu\text{m}$ band will also be useful for air pollution studies and will improve numerous products that rely on clear-sky radiances (i.e., land and sea surface products).

During the daytime, the $0.64\text{-}\mu\text{m}$ band will assist in the detection of fog, estimation of solar insolation (Diak et al. 1998), and depiction of diurnal aspects of clouds. The $0.64\text{-}\mu\text{m}$ visible band is also used for daytime snow and ice cover, detection of severe weather, low-level cloud-drift winds, smoke, volcanic ash, hurricane analysis, and winter storm analysis. A similar band on the current GOES imager has demonstrated many of these applications, although the ABI will have a factor of 4 improved spatial resolution. Images of lake-effect snowbands are shown for a number of spatial resolutions in Fig. 4. Note the finer features in the 0.5-km data (upper-right panel) as opposed to either (MODIS or GOES) 1-km data (lower panels).

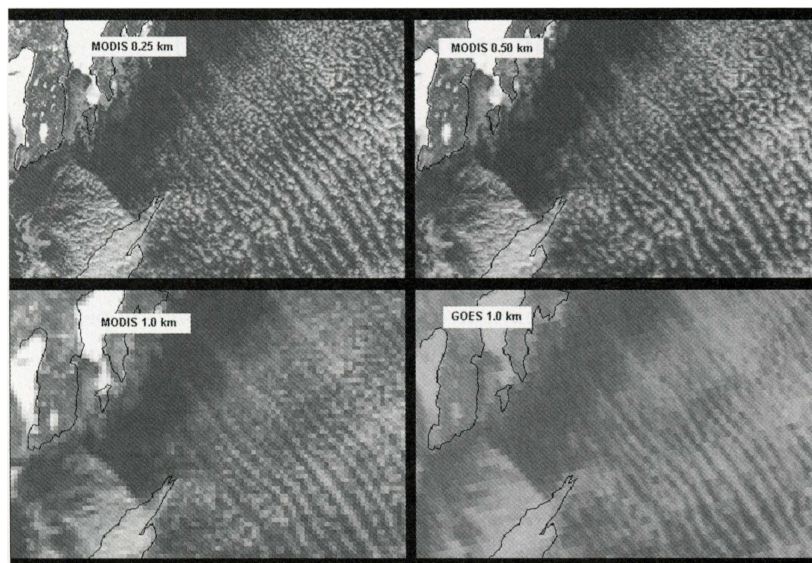


FIG. 4. MODIS visible band (no. 1) at three different spatial resolutions (with GOES) showing lake-effect cloud bands over Lake Superior at 1720 UTC 19 Jan 2001. (upper right) The finer 0.5-km spatial resolution of the ABI simulation allows a better depiction of the cloud and lake ice features than either the 1.0-km MODIS or GOES data. All four images have been remapped to the GOES perspective.

Near-infrared bands. The $0.865\text{-}\mu\text{m}$ band, along with the $0.64\text{-}\mu\text{m}$ band, will be used for detecting daytime clouds, fog, and aerosols, and calculating a normalized difference vegetation index (NDVI). This band can help in determining vegetation amount, estimating aerosol properties, and studying ocean characteristics. The current GOES lone visible channel (approximately $0.65\text{ }\mu\text{m}$) does not delineate burn scars, thus, this band on ABI has potential for detecting forest regrowth patterns. As demonstrated with *Meteosat-8* data, it is anticipated that low-level winds may be derived from time sequences of $0.865\text{-}\mu\text{m}$ images, especially over the water (Schmetz et al. 2002).

The $1.378\text{-}\mu\text{m}$ band will detect very thin cirrus clouds during the day (Gao et al. 2002). This band is centered in a strong water vapor absorption spectral region. It does not sense the lower troposphere and thus provides excellent daytime sensitivity to high, very thin cirrus under most circumstances. Correction for the presence of contrail and thin cirrus, which are possible with this band, is important when estimating many surface parameters. However, when the total precipitable water (TPW) is less than approximately 10 mm, reflectance from the surface mitigates the benefits of this band for thin cirrus detection (Sieglaff and Schmit 2003).

In conjunction with other bands, the $1.6\text{-}\mu\text{m}$ band will be used for daytime cloud/snow/ice discrimina-

tion, total cloud cover estimation, cloud-top phase (Hutchison 1999), and smoke detection from low-burn-rate fires. The $1.6\text{-}\mu\text{m}$ band has a relatively large difference between the imaginary refraction components between water and ice (Baum et al. 2000) that makes daytime water/ice cloud delineation possible; this will be very useful for aircraft routing.

The $2.25\text{-}\mu\text{m}$ band, in conjunction with other bands, will enable cloud particle size estimation; cloud particle growth is an indication of cloud development and intensity of that development (Kaufman et al. 1997). Other applications of the $2.25\text{-}\mu\text{m}$ band include use in a multispectral approach for aerosol particle size estimation (by characterizing the aerosol-free background

over land), cloud screening, hot-spot detection, snow detection, and total moisture determination. The MODIS cloud mask algorithm uses a similar band (Ackerman et al. 1998).

Infrared bands. The shortwave IR window ($3.9\text{ }\mu\text{m}$) band (on the current GOES imagers) has been demonstrated to be useful in many applications, including fog/low cloud identification at night (Ellrod et al. 1998), fire/hot-spot identification (Prins et al. 1998), volcanic

eruption and ash detection, and daytime snow and ice detection. This band is also useful for studying urban heat islands due to Planck radiance–increased temperature sensitivity at shorter wavelengths. In addition, this band will be used to study clouds.

The 6.2 and $7.0\text{-}\mu\text{m}$ bands will be used for upper-level tropospheric water vapor tracking, jet stream identification, hurricane track forecasting, midlatitude storm forecasting, severe weather analysis, and upper-level moisture estimation (Soden and Bretherton 1993; Moody et al. 1999; Weldon and Holmes 1991). The improved spatial resolution of the ABI is demonstrated in Fig. 5. The “herring bone pattern,” evident in the higher spatial resolution data, is revealing moisture structure; this scene was completely clear (with the exception of some low fog), but there was moderate/severe turbulence over this region.

The $7.3\text{-}\mu\text{m}$ band reveals information about mid- and lower-level atmospheric flow and can help identify jet streaks. It has been proven to be useful in identifying and tracking volcanic plumes due to SO_2 absorption (Realmuto et al. 1997). Vertical moisture information can be gained from comparison of measurements in all three (6.2, 7.0, and $7.3\text{ }\mu\text{m}$) water vapor bands.

The $8.5\text{-}\mu\text{m}$ band has been used in combination with the 11.2- , and $12.3\text{-}\mu\text{m}$ bands to derive cloud-top phase (Strabala et al. 1994). This determination of the microphysical properties of clouds includes a more accurate and consistent delineation of ice clouds from water clouds during the day or night. The same three spectral bands enable detection of volcanic dust

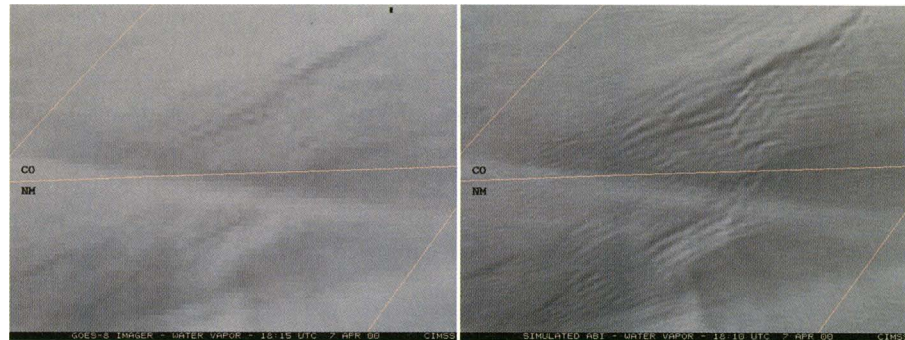


FIG. 5. Current GOES imager and simulated ABI (using MODIS) water vapor band images of mountain waves over Colorado and New Mexico on 7 Apr 2000. The improved spatial resolution of the water vapor bands of the ABI allows a better depiction of the mountain wave features in this cloud-free scene (all the structure seen is due to mesoscale variability of midtropospheric water vapor). These mountain waves were induced by strong northwesterly flow associated with a pair of upper-tropospheric jet streaks moving across the elevated terrain of the southern and central Rocky Mountains. The mountain waves appear better defined over Colorado, where aircraft reported moderate to severe turbulence.

clouds containing sulfuric acid aerosols (Realmuto et al. 1997; Ackerman and Strabala 1994). Other uses of the $8.5\text{-}\mu\text{m}$ band include thin cirrus detection in conjunction with the $11.2\text{-}\mu\text{m}$ band (thus improving other products by reducing cloud contamination), better atmospheric moisture correction in relatively dry atmospheres in conjunction with the $11.2\text{-}\mu\text{m}$ band (thus improving sea surface temperature measurements), and estimation of surface properties in conjunction with the $10.35\text{-}\mu\text{m}$ band.

The thermal ozone band at $9.6\text{ }\mu\text{m}$ will provide information both day and night about the dynamics of the atmosphere near the tropopause with both high spatial and temporal resolutions (Li et al. 2001; Schmidt et al. 2004). Significant wind shear, turbulence, and tropopause folding occur in the midlatitudes, particularly during the baroclinic storms in the spring and fall. A high temporal and spatial ozone product derived from the $9.6\text{ }\mu\text{m}$ may give some indications to clear-air turbulence.

The $10.35\text{-}\mu\text{m}$ atmospheric window band is less sensitive to low-level moisture and, hence, helps with atmospheric moisture corrections, cloud particle size, and surface properties. Chung et al. (2000) demonstrated the importance of the $10\text{--}11\text{-}\mu\text{m}$ spectral region for determining particle sizes in ice clouds.

The longwave infrared window ($11.2\text{ }\mu\text{m}$) band provides day/night cloud analyses for general forecasting and broadcasting applications, precipitation estimates (Vicente et al. 1998), severe weather analyses, cloud-drift winds (Velden et al. 1998a), hurricane strength (Velden et al. 1998b; Kossin 2002)

and track analyses, cloud-top heights, volcanic ash detection (Prata 1989), fog detection in multiband products (Lee et al. 1997), winter storms, and cloud phase/particle size estimates in multiband products. A convective storm observed by both MODIS and the current GOES imager is shown in Fig. 6 to demonstrate the improvement anticipated with the ABI spatial resolution. The “warm wake” or “enhanced V”

is much more evident in the higher-resolution data (McCann 1983). Also, concentric circles, indicating cloud-level gravity waves, are seen in the higher spatial resolution ABI data, but not the poorer spatial resolution GOES data. It is possible that these waves could be used as an indicator of turbulence. The MODIS data were averaged to 2 km to simulate the spatial resolutions of the ABI.

The 12.3- μm band offers nearly continuous monitoring for numerous applications, including low-level moisture determinations, volcanic ash identification (Davies and Rose 1998), sea surface temperature (SST) measurements (Wu et al. 1999), and cloud particle size estimates (from multiband applications). Dunion and Velden (2004) have shown that mid-level dust amounts (from the Saharan air layer) can be useful in determining hurricane intensification in the Atlantic basin.

The 13.3- μm band is used for cloud-top height assignments of cloud-drift motion vectors, high-cloud products supplementing Automated Surface Observing System (ASOS) observations (Schreiner et al. 1993; Wylie and Menzel 1999), tropopause delineation, and estimation of cloud opacity. ABI cloud products will be further improved by combining the data with high spectral resolution sounder data from the HES (Li et al. 2004a,b); these will be useful for aviation weather forecasters, numerical weather prediction (for analysis and/or validations), and possibly determination of ash cloud heights for the Volcanic Ash Advisory Center (VAAC). Products using the 13.3 μm band are being demonstrated with the GOES-12/-N/-O/-P imagers (Schreiner and Schmit 2001; Hillger et al. 2003).

Meteosat-8 data, and ABI simulated data from MODIS, AIRS, and forward model calculations, are being used to prepare for ABI. Some of the imager products and the primary and secondary bands used to compute those products are listed in Table 3. In the table, “HES” refers to a product from the combined imager/HES

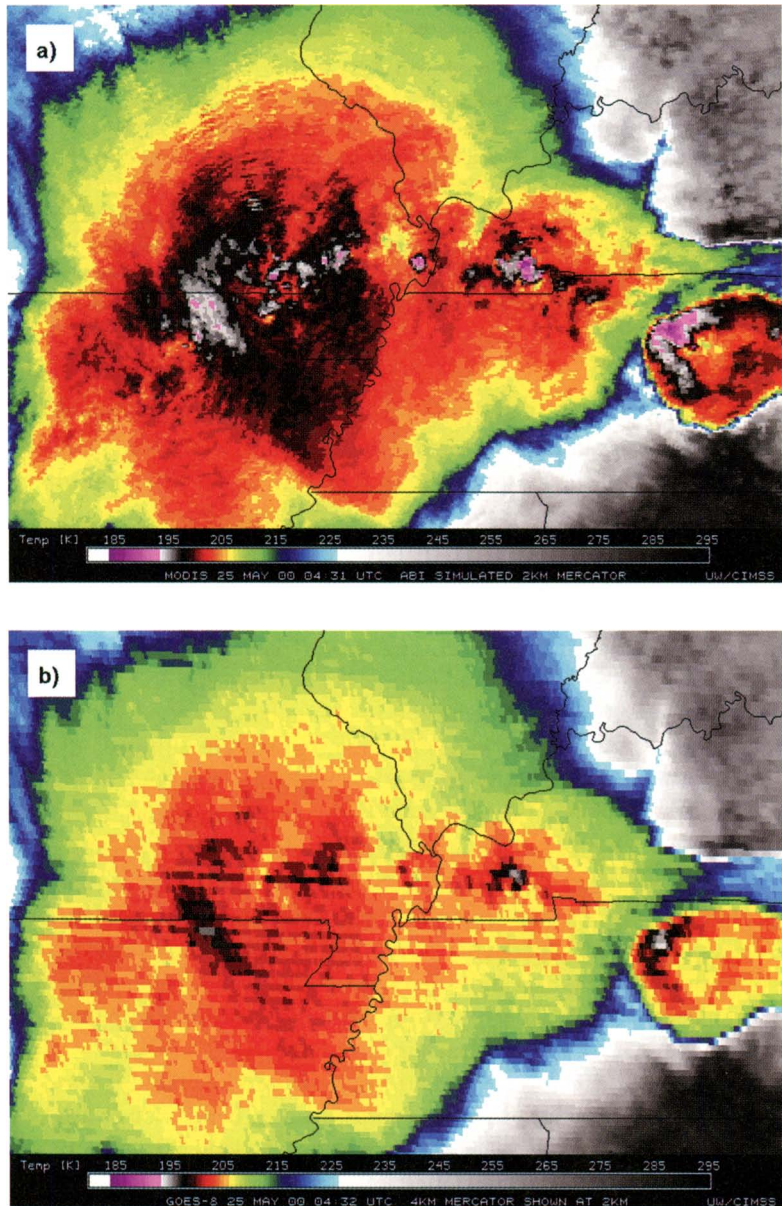


FIG. 6. Improved spatial resolution of the infrared window bands of the ABI demonstrated from MODIS data (a) for a convective cloud case. Note the colder cloud-top brightness temperatures and the sharper “Enhanced V” signature located over central Tennessee on 25 May 2000. Also of interest are the concentric anvil-layer waves observable in the higher spatial resolution IR data, associated with rapidly intensifying convection along the Missouri/Arkansas border region. These are not evident in (b), the current GOES imager data.

TABLE 3. Selected imager products and needed spectral coverage from the ABI. The columns labeled HES reflect products that can be improved with high spectral infrared data from the SND or CW instruments.

Sample product list	Primary ABI band(s) (μm)	Secondary ABI band(s) (μm)	HES SND	HES CW
Aerosols/dust/smoke	0.47, 2.2, 8.5, 12.3	0.64, 0.865, 1.6, 10.3, 11.2	Yes	Yes
Clear-sky masks	0.64, 1.38, 8.5, 11.2, 12.3	0.47, 0.865, 1.6, 8.5, 13.3		
Cloud imagery	0.64, 1.38, 3.9, 11.2, 13.3	0.865, 8.5, 10.35	Yes	
Cloud-top: . . . Microphysics	0.64, 1.6, 3.9, 10.35, 11.2	0.865, 2.2, 8.5	Yes	
. . . Phase	1.6, 8.5, 11.2, 13.3	0.6, 1.38, 2.2	Yes	
. . . Pressure/temperature	8.5, 11.2, 13.3	3.9, 6.15, 7, 10.3	Yes	
Fires/hot spots	3.9, 11.2	0.64, 2.2, 12.3, 13.3		Yes
Fire burn scars	0.865	0.64, 10.3		Yes
Hurricane intensity	11.2	0.64, 3.9, 6.15, 8.5, 13.3	Yes	
Insolation	0.47, 0.64	0.865, 1.6		
Land skin temperature	3.9, 11.2, 12.3	7.3, 8.5, 10.3	Yes	
Low cloud and fog	3.9, 11.2	0.64, 1.61, 10.3, 12.3	Yes	
Rainfall rate/QPE	8.5, 11.2, 12.3, 13.3	0.64, 6.15, 7.3, 10.3	Yes	
Derived motion	0.64, 3.9, 6.19, 7, 7.3, 11.2	0.865, 1.38, 9.6, 10.3, 12.3, 13.3	Yes	
Sea ice products	0.64, 1.6	2.2, 3.9, 11.2, 12.3		
Sea surface temperature	3.9, 11.2, 12.3	8.5, 10.35	Yes	
Snow detection (cover)	1.61	0.64, 0.865, 2.2, 3.9, 11.2		Yes
SO_2 (upper level)	8.5, 7.34	9.6, 11.2, 13.3	Yes	
Surface properties	8.5, 10.35	11.2	Yes	
Suspended sediment	0.64, 0.865	0.47		Yes
Total ozone	9.6	11.2, 13.3	Yes	
Turbulence	6.15, 7, 9.6	7.3, 11.2, 13.3		
Vegetation index	0.64, 0.865	2.2		Yes
Volcanic ash product	0.64, 3.9, 8.5, 12.3	7.3, 11.2, 13.3	Yes	

sounder (SND) or coastal waters (CW) system. Table 4 shows a summary of the characteristics of the current imager and ABI. The specified instrument noise for most bands is 0.1 K (although the 13.3- μm band is 0.3 K), all referenced at 300 K. The ABI is also expected to have on-orbit visible calibration, while the current GOES instruments do not. This on-orbit calibration not only improves the calibration, but also allows for monitoring any calibration changes more rapidly. Improved visible calibration will minimize the degradation over time that the current visible sensors demonstrate. Improved calibration will allow for more accurate composites of images from several sensors.

An example of “16 band” ABI multiple panel image from 1300 UTC 11 April 2004 is presented in Fig. 7. This image over France is compiled from measurements from three separate satellite instruments

(MODIS, *Meteosat-8*, and AIRS). MODIS data were used to simulate bands 1–4, 6, 7, 11, 12, and 14–16. *Meteosat-8* was used for bands 5 and 8, while AIRS data were used for bands 9, 10, and 13. The spectral simulation is more representative for those bands derived from the high spectral resolution AIRS data due to convolution. The spatial information is more representative for those bands derived from higher spatial resolution MODIS data. The 1.378- μm band is dark because it is centered within an absorption band. Note that the snow-covered Alps are bright (reflective) in the first three visible bands, while darker (absorbing) in both the 1.6- and 2.2- μm bands. ABI will generate similar multispectral observations every 5 (for CONUS imagery) or at least 15 (for FD imagery) min.

PRODUCTS. Examples of ABI products are presented in the broad categories of imagery/radiances,

TABLE 4. Comparison of the current and future U.S. geostationary imagers. It should be noted that the instrument noise values for ABI are specifications, while those from the GOES imager are on-orbit measurements.

Parameter	Current GOES imager	Future GOES imager	Comments
Visible bands	1	2	Cloud cover, plant health, and surface features during the day, etc.
Near-IR bands	0	4	Cirrus clouds, low cloud/fog and fire detection, etc.
Infrared bands	4	10	Upper-level water vapor, clouds, SO_2 , SST, etc.
Coverage rate	25 min for full disk	Approximately 5 min for full disk	Approximately 5 times faster
Noise (at 300 K) in the IR window	0.15 K	0.10 K	No correction has been made for the larger FOV of the current GOES imager compared to that of the ABI
Navigation	4 km (day) 6 km (night)	<2 km (day) <3 km (night)	
Spatial resolutions of the infrared bands	4–8 km	2 km	At the subsatellite point
On-orbit visible calibration	No	Yes	

atmospheric products, oceanographic products, land products, and hazard detection.

Imagery radiances. The ABI bands, when displayed as a time series of images, will offer a multitude of applications. For example, the current GOES imager

water vapor band ($6.5/6.7 \mu\text{m}$) can be used to estimate upper-level moisture (Soden and Bretherton 1993; Moody et al. 1999) and define upper-level jet streaks (Weldon and Holmes 1991). The finer spatial resolutions of the water vapor bands will allow for the monitoring of finer-scale phenomena. Multispectral ABI displays in band differences or principal component analysis (Hillger 1996) will enable even more applications. For example, the difference between the 11- and 12- μm BTs, known as the split window, helps detect dust, volcanic ash plumes, low-level moisture, and skin temperature, and aids in distinguishing between cloud types and biomass-burning aerosols (Ackerman 1996; Ackerman and Chung 1992; Moeller et al. 1996; Prata 1989; Barton et al. 1992; Hayden et al. 1996; Prins et al. 1998); outflow boundaries have also been observed in these images (Dostalek et al. 1997). The ABI not only returns the 12- μm band after its absence on the GOES-12/-N/-O/-P imagers, but also adds another win-

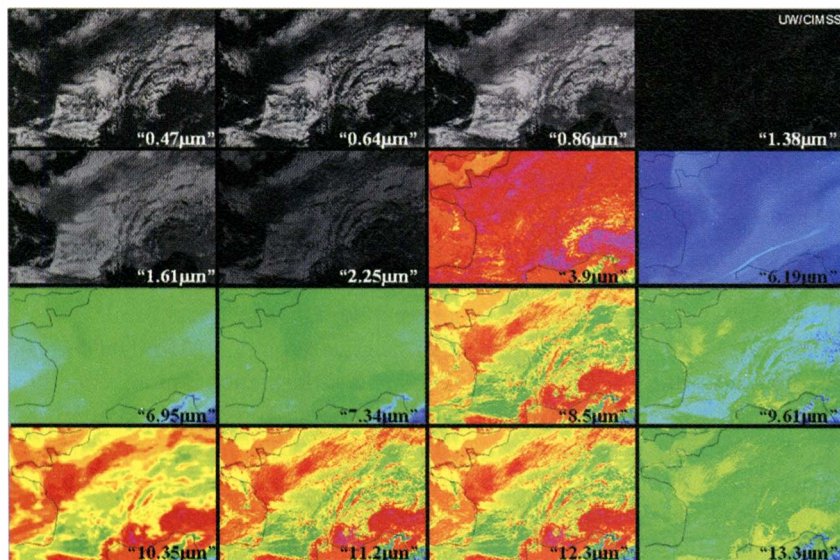


FIG. 7. A simulated “16-band” ABI multiple panel image at 1300 UTC 11 Apr 2004. This image over France is built from measurements from three separate satellite instruments (MODIS, Meteosat-8, and AIRS). For the IR bands, the blue and green colors correspond to the coldest temperatures, while the orange and red colors correspond to the warmest temperatures.

dow band at $10.35\text{ }\mu\text{m}$ to allow for additional quality control on products that currently only use two bands. The difference between the 6.7 - and the $11\text{-}\mu\text{m}$ BTs has been shown to be correlated to convection (Mosher 2001). The enhanced spatial and temporal resolutions of the ABI will allow for improved monitoring of convection.

Spatially averaged clear-sky BTs are produced from the imagers for inclusion in numerical models. For example, the direct assimilation of water vapor (WV) clear-sky brightness temperatures (CSBT) from *Meteosat-7* became operational at the European Centre for Medium-Range Weather Forecasts (ECMWF) in April 2002 using the four-dimensional variational data assimilation (4DVAR) system. ECMWF is also assimilating the hourly water vapor band from the imagers on GOES-9, -10, and -12 (Szyndel et al. 2003). The Canadian Meteorological Centre also assimilates radiances from the GOES imagers, including infrared window bands (Garand 2003). Research has also been done on directly assimilating GOES imager BTs (Raymond et al. 2004). The GOES CSBT product will be improved for ABI, due to a superior cloud mask, a higher signal-to-noise ratio, and more spectral bands representing different layers of the Earth-atmosphere system. ABI radiances will be used to derive a cloud mask that separates clear-from cloudy-sky radiances; the algorithm will start with advanced spectral and spatial tests, such as those used in the MODIS cloud mask (Ackerman et al. 1998), and will supplement these with temporal consistency tests. ABI will also have more bands for assimilation in numerical models.

Atmospheric products. Cloud products generated via the CO_2 absorption technique have been demonstrated from instruments on both geostationary and polar-orbiting platforms (Schreiner et al. 1993; Wylie et al. 1994; Wylie and Wang 1997; Wylie and Menzel 1999; Frey et al. 1999; Schreiner et al. 2001). Cloud products derived from the GOES sounder have been used to initialize numerical models (Kim and Benjamin 2000; Bayler et al. 2000). Improved cloud products from ABI will include cloud-top pressure/height, effective cloud amount (representative of cloud optical thickness), and cloud-top temperature. In addition, several new bands on ABI will allow estimation of cloud-top particle size and cloud phase. Using techniques demonstrated with MODIS (Platnick et al. 2003), cloud and surface classifications will be generated (Li et al. 2003). ABI cloud products will also be computed in conjunction with information from

HES (Li et al. 2002). The high spectral observations of the HES will allow for an improved initial estimate of the cloud height and effective amount to be used with the ABI data.

Rainfall estimation techniques (Scofield and Kuligowski 2003), such as the hydro-estimator (Vicente et al. 1998), rely on the infrared window; multispectral approaches such as the GOES Multispectral Rainfall Algorithm (GMSRA) offer complementary information regarding light rainfall (Ba and Gruber 2001). These satellite rainfall estimations will be improved with the ABI higher spatial resolution (better depiction of cold cores), more frequent images (improved cell growth information), improved cloud heights (with multiple bands and HES), introduction of cloud phase (new ABI bands), better signal-to-noise ratios, and better navigation/registration. For example, the time tendency of BTs and cloud-top particle size can be used to help categorize cell growth. The time tendency of BTs can also be used to monitor storm initiation and growth (Roberts and Rugledge 2003).

The tracking of atmospheric features (Velden et al. 1997) will be enhanced using ABI data with a higher spatial resolution (better edge detection), more frequent images (offers different time intervals), a better cloud height detection (with multiple bands), additional new bands (0.865 and $1.378\text{ }\mu\text{m}$), better signal-to-noise ratio, and better image navigation/registration. Currently, the atmospheric motion height assignment is one of the greatest sources of error (Nieman et al. 1993); these errors will be reduced with data from ABI coupled with HES.

Determination of hurricane location and intensity (Velden et al. 1998a,b; Goerss et al. 1998; Bosart et al. 2000) are well-established GOES imager products. The Objective Dvorak Technique (ODT) relies on the longwave infrared window band to monitor the strength of tropical cyclones (Velden et al. 1998a). This product will be improved with better ABI temporal and spatial resolutions; it is estimated that increased ability to detect warming in the eye and detailed structure in the cold eyewall region may lead to ODT improvements of up to half a category (M. DeMaria 2004, personal communication). ABI, in conjunction with HES, will also allow investigation of multispectral approaches for estimating hurricane intensity.

The routine high spatial resolution and “rapid” scan imagery from ABI will also have many applications, especially in the realm of severe storm monitoring (Purdom 1976). When the current imager goes into rapid or superrapid scan mode, this limits

cover in other locations, for example, in the Southern Hemisphere. With the ABI, routine coverage can continue uninterrupted while taking mesoscale sectors every 30 s.

Oceanographic products. The GOES platform enables frequent measurements of a given area with the same viewing angle. SST from the GOES imager (Wu et al. 1999; Legeckis et al. 2002) have been shown to have better coverage than those from polar-orbiting AVHRR as persistent viewing enables more cloud-free measurements of a given area. The ABI will allow for even more rapid viewing, giving more looks at a given region to find enough suitably clear radiances. The GOES SST has applications ranging from weather forecasting to fisheries management (Seki et al. 2001). Time animation of GOES SST fields (to deduce regions of stronger currents) have also been used for safe oil and gas operations in the Gulf of Mexico (Walker et al. 2003). ABI SST will be improved through higher spatial resolution, more frequent images, more spectral bands, better atmospheric correction (in part with data from HES), better cloud and aerosol detection, and less instrument noise.

Suspended sediments in coastal waters can be detected with a 0.865- μm band (Aquirre-Gomez 2000). While these estimates would not be as fine as that from the anticipated visible/near-infrared HES-CW imaging function, the ABI-based estimate could be

used to help determine either where the HES-CW should scan or possibly to monitor changes between HES-CW observations.

Hazards. Detection of volcanic ash plumes is important for aviation (Casadevall 1992; Davies and Rose 1998; Hillger and Clark 2002; Ellrod 2001). ABI volcanic ash detection will rely on 12- μm data (Schmit et al. 2001) that are combined with 7.34- and 8.5- μm data. The ABI water vapor bands have been shifted to detect upper-level SO₂, as well as midlevel water vapor; line-by-line radiative transfer calculations (Hannon et al. 1996) in Fig. 8 show the sensitivity of the 7.34- and 8.5- μm bands to SO₂ for the *U.S. Standard Atmosphere, 1976*. If the vertical and spatial extents of the plume are sufficient, ABI should be able to detect medium to large SO₂ amounts [greater than 100 Dobson units (DU)] but probably not small amounts (less than approximately 50 DU). High spectral resolution measurements in the 7- μm region should have more sensitivity than broadband measurements for detecting SO₂ because individual absorption features can be detected, thus synergy with the HES sounder will be a key with this product. ABI bands, simulated from AIRS data from 13 July 2003, show the potential for depicting upper-level SO₂. Figure 9 shows the SO₂ plume from the eruption of Montserrat, West Indies. This figure shows a brightness temperature difference image for two ABI spectral bands, one of which has no sensitivity to SO₂. Independent SO₂ retrievals (not shown) from both AIRS and the Total Ozone Mapping Spectrometer (TOMS) show amounts between 100 and 500 DU for this case.

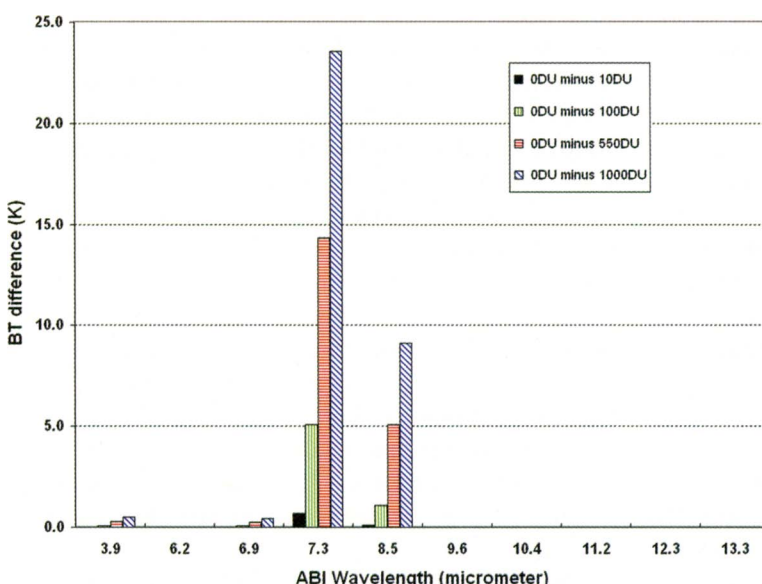


FIG. 8. Forward model calculations of ABI brightness temperature differences caused by different amounts of SO₂. The ordinate is the difference between calculated atmospheres with no SO₂ and those with different amounts of SO₂.

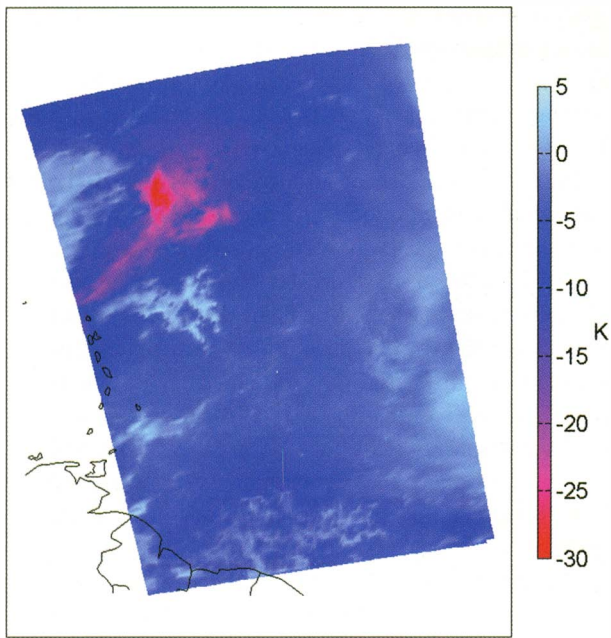


FIG. 9. AIRS data (1700 UTC 13 Jul 2003) over the Caribbean convolved with ABI 7.34- and 13.3- μm band spectral response functions to simulate the spectral characteristics of the two ABI bands. A difference image is shown between the 7.34- and 13.3- μm bands. The image shows the location of a SO_2 plume in magenta to red shades.

imager; ABI offers both improved spatial and temporal measurements, along with improved radiometrics and image navigation. For example, Fig. 10 shows the 4- and 11- μm band difference for the GOES-10 imager and the simulated ABI from MODIS (which has similar noise characteristics as the ABI). The ABI image (from MODIS) shows greater detail in the structure of fog/stratus than the GOES-10 image. Both images are shown in the GOES projection.

Areas of supercooled water clouds that could produce aircraft icing (Ellrod 1996) have been highlighted using GOES imager split window (11- μm band minus 12- μm band) BT differences. The ABI addition of 1.6- and 8.5- μm bands will improve this product both during the day and night. The improved spatial and temporal resolutions of the ABI will also allow for a clearer depiction of the cloud-top microphysical properties.

Daytime smoke/aerosols and, hence, air quality will be detectable using the ABI 0.47- μm band at high temporal resolutions. Due to the episodic nature of these events, the improved temporal scans from the geostationary perspective are necessary.

Land products. Detection of active fires using the 3.9- and 11- μm bands (Prins et al. 1998) will be improved

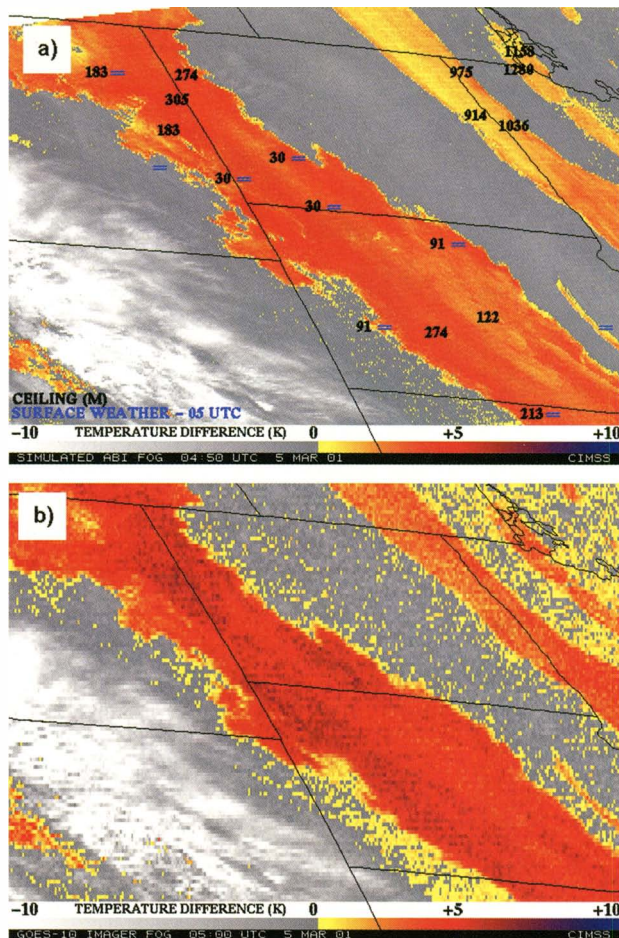


FIG. 10. Fog detection with 4–11 μm for the simulated (a) ABI and (b) GOES-10 imager. Both images are from 5 Mar 2001. Note the better depiction of the fog in the simulated ABI image. Surface weather and cloud ceilings are also plotted on the simulated ABI image.

by ABI spatial and temporal resolutions along with hotter maximum temperatures detectable in these bands. The geostationary perspective enables diurnal monitoring of fires. Fire locations and characteristics can then be used to improve air quality/visibility forecasts.

Diurnal monitoring of vegetation trends and health, similar to the global AVHRR vegetation monitoring (Kogan 1990; Tarpley et al. 1984), will be possible with the ABI 0.865- μm band (in tandem with the 0.64 μm). While the polar orbiters only allow a few views per day (at different viewing geometry), the ABI will offer many views (at the same viewing angles). These multiple looks increase the chance of obtaining a clear surface depiction. ABI will be able to monitor localized vegetation stress, help to estimate fire danger, and detect fire burn scars. In smoke-affected regions the ABI 2.25- μm band will enable an improved NDVI

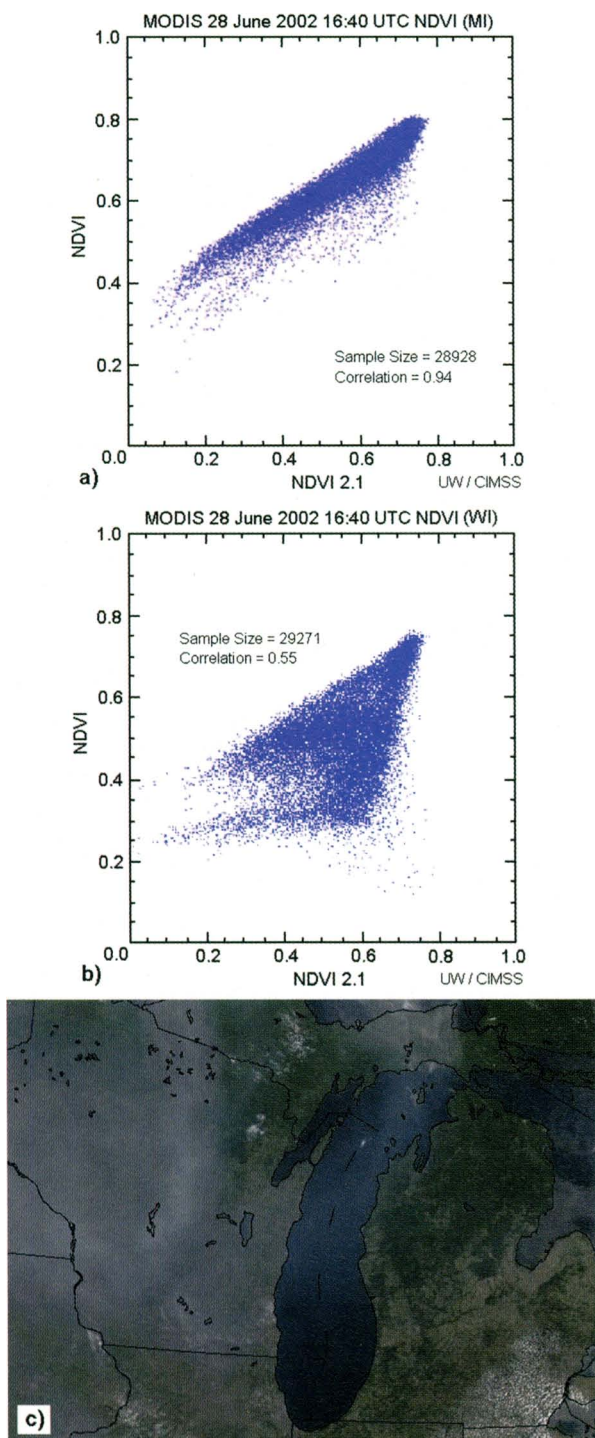


FIG. 11. NDVI from MODIS data at 1640 UTC 28 Jun 2002. (a) The traditional NDVI (using 0.86- and 0.64- μm measurements) on the ordinate compared to a smoke insensitive NDVI (using 2.1 and 0.64- μm) on the abscissa for a clear scene; (b) The same for a smoky scene. The traditional NDVI is affected by smoke. (c) A MODIS “natural color” image for these regions of interest; note the thick smoke over Wisconsin, transported southward from wildfires burning in northern Saskatchewan, Canada.

product (Karnieli et al. 2001) since this band is much less sensitive to smoke than the 0.64- μm band (smoke backscatters more solar radiation at shorter wavelengths). Figure 11a shows an NDVI calculated with the MODIS 2.1- μm band in a smoke-free region that is highly correlated (correlation coefficient of 0.94) to the traditional NDVI product, but less correlated (correlation coefficient of 0.55) in regions of smoke (Fig. 11b). A MODIS “natural color” image shows the smoke over Wisconsin, west of Lake Michigan (Fig. 11c), but not over lower Michigan. Replacing shorter wavelengths, such as 0.64 μm , with a longer wavelength, such as 2.1 or 2.25 μm , results in an NDVI that is much less sensitive to smoke. Thus, to develop NDVI from ABI data, a multispectral approach that incorporates the 0.64-, 0.865-, and the 2.1- μm bands may prove to be optimal.

The skin temperature or land surface temperature (LST) will also be produced from a combination of information from the HES sounder measurements, along with the various window measurements from the ABI. In clear skies, the diurnal signature will be monitored (Hayden et al. 1996). Temperature contrasts between cities, larger lakes, and, possibly, regions of different vegetation will be apparent. The LST estimates from the GOES-R series will be improved over that from the current GOES series. This is in part due to the improved spatial resolutions, additional window channels, and combination with high spectral measurements. Another surface product that will be produced from ABI data will be the surface albedo.

Snow and ice cover, under clear conditions, will also be monitored with the ABI. Again, the improved spatial, spectral, temporal, radiometric, and image navigation improvements will improve the estimates of these products.

SUMMARY. ABI represents an exciting expansion in geostationary remote sensing capabilities and will be used for a wide range of weather, oceanographic, climate, and environmental applications. ABI addresses the needs of the many users of geostationary data by increasing spatial resolution (to better monitor small-scale features), scanning faster (to improve temporal sampling and to scan additional regions), and adding spectral bands (to enable new and improved products for a wide range of phenomena). Every product that is being produced from the current GOES imager will be improved with data from the ABI. In addition, several new products will be possible that exploit the improved spectral, temporal, and spatial resolutions. Datasets compiled from both

operational and research satellites are being used to prepare for the use of the ABI data.

Where appropriate, products will be generated from combined ABI high spatial and HES high spectral resolution data. Given the fast coverage rate of the ABI, temporal collocations with HES data should be better than 5 min. Current MODIS/AIRS investigations are revealing possible future ABI/HES synergies. The GOES-R series will be an integral part of the Global Earth Observation System of Systems (GEOSS).

ACKNOWLEDGMENTS. The authors wish to thank a host of scientists at CIMSS, NOAA/NESDIS, NASA, and other agencies that contributed to ABI band selection. This includes S. Ackerman, B. Baum, D. Chesters, M. Coakley, G. Ellrod, D. Flanagan, R. Frey, M. K. Griffin, L. Gumley, A. Heidinger, R. Heymann, D. Hillger, A. Huang, B. Kuligowski, C. Moeller, F. Mosher, J. P. Nelson III, A. Neuendorffer, F. Prata, E. Prins, R. Rabin, J. Schmetz, C. Schmidt, A. Schreiner, K. Strabala, C.-Y. Liu, M. Weinreb, and H. Woolf. Former University of Wisconsin—Madison undergraduate students J. Sieglaff and K. Karnauskas are also thanked for their work with the AVIRIS, MODIS, and AIRS data. The authors would like to also thank the entire GOES-R team from government, academia, and industry. The simulated ABI Spectral Response Files are available upon request. The GOES-R cost–benefit study is online at www.osd.noaa.gov/goes_R/docs/GOES-R_CBA_Final_Jan_9_2003.pdf. The authors would like to thank the three anonymous reviewers of this manuscript. More information on the specifications for the ABI can be found online at <http://goespoes.gsfc.nasa.gov/goes/index.html>. This work was supported under grant NA07EC0676. The views, opinions, and findings contained in this paper are those of the authors and should not be construed as an official National Oceanic and Atmospheric Administration or U.S. government position, policy, or decision.

REFERENCES

- Ackerman, S. A., 1996: Global satellite observations of negative brightness temperature differences between 11 and $6.7\text{ }\mu\text{m}$. *J. Atmos. Sci.*, **53**, 2803–2812.
- , and H. Chung, 1992: Radiative effects of airborne dust on regional energy budgets at the top of the atmosphere. *J. Appl. Meteor.*, **31**, 223–236.
- , and K. I. Strabala, 1994: Satellite remote sensing of H_2SO_4 aerosol using the 8 to $12\text{ }\mu\text{m}$ window region: Application to Mount Pinatubo. *J. Geophys. Res.*, **99**, 18 639–18 649.
- , —, W. P. Menzel, R. A. Frey, C. C. Moeller, and L. E. Gumley, 1998: Discriminating clear sky from clouds with MODIS. *J. Geophys. Res.*, **103**, 32 141–32 157.
- Aquirre-Gomez, R., 2000: Detection of total suspended sediments in the North Sea using AVHRR and ship data. *Int. J. Remote Sens.*, **21**, 1583–1596.
- Aumann, H. H., and Coauthors, 2003: AIRS/AMSU/HSB on the Aqua mission: Design, science objectives, data products, and processing systems. *IEEE Trans. Geosci. Remote Sens.*, **41**, 253–264.
- Ba, M., and A. Gruber, 2001: GOES Multispectral Rainfall Algorithm (GMSRA). *J. Appl. Meteor.*, **40**, 1500–1514.
- Barton, I. J., A. J. Prata, I. G. Watterson, and S. A. Young, 1992: Identification of the Mount Hudson volcanic cloud over SE Australia. *Geophys. Res. Lett.*, **19**, 1211–1214.
- Baum, B. A., P. F. Soulen, K. I. Strabala, M. D. King, S. A. Ackerman, W. P. Menzel, and P. Yang, 2000: Remote sensing of cloud properties using MODIS Airborne Simulator imagery during SUCCESS. II. Cloud thermodynamic phase. *J. Geophys. Res.*, **105**, 11 781–11 792.
- Bayler, G. M., R. M. Aune, and W. H. Raymond, 2000: NWP cloud initialization using GOES sounder data and improved modeling of nonprecipitating clouds. *Mon. Wea. Rev.*, **128**, 3911–3920.
- Bosart, L. F., C. S. Velden, W. E. Bracken, J. Molinari, and P. G. Black, 2000: Environmental influences on the rapid intensification of Hurricane Opal (1995) over the Gulf of Mexico. *Mon. Wea. Rev.*, **128**, 322–352.
- Casadevall, T. J., 1992: Volcanic hazards and aviation safety: Lessons of the past decade. *FAA Aviation Safety J.*, **2** (3), 1–11.
- Chung, S., S. Ackerman, and P. F. van Delst, 2000: Model calculations and interferometer measurements of ice-cloud characteristics. *J. Appl. Meteor.*, **39**, 634–644.
- Davies, M. A., and W. I. Rose, 1998: Evaluating GOES imagery for volcanic cloud observations at the Soufrière Hills volcano, Montserrat. *Eos, Trans. Amer. Geophys. Res.*, **79**, 505–507.
- Diak, G. R., M. C. Anderson, W. L. Bland, J. M. Norman, J. M. Mecikalski, and R. A. Aune, 1998: Agricultural management decision aids driven by real time satellite data. *Bull. Amer. Meteor. Soc.*, **79**, 1345–1355.
- Dostalek, J. F., J. F. Weaver, J. F. W. Purdom, and K. Y. Winston, 1997: Picture of the quarter: Nighttime detection of low-level thunderstorm outflow using a GOES multispectral image product. *Wea. Forecasting*, **12**, 947–950.
- Dunion, J. P., and C. S. Velden, 2004: The impact of the Saharan air layer on Atlantic tropical cyclone activity. *Bull. Amer. Meteor. Soc.*, **85**, 353–365.

- Ellrod, G. P., 1996: The use of GOES-8 multispectral imagery for the detection of aircraft icing regions. Preprints, *Eighth Conf. on Satellite Meteorology and Oceanography*, Atlanta, GA, Amer. Meteor. Soc., 168–171.
- , 2001: Loss of the 12.0 μm “split window” band on GOES-M: Impacts on volcanic ash detection. Preprints, *11th Conf. on Satellite Meteorology and Oceanography*, Madison, WI, Amer. Meteor. Soc., CD-ROM, P1.15.
- , R. V. Achutuni, J. M. Daniels, E. M. Prins, and J. P. Nelson III, 1998: An assessment of GOES-8 imager data quality. *Bull. Amer. Meteor. Soc.*, **79**, 2509–2526.
- Frey, R. A., B. A. Baum, W. P. Menzel, S. A. Ackerman, C. C. Moeller, and J. D. Spinhime, 1999: A comparison of cloud top heights computed from airborne LIDAR and MAS radiance data using CO₂-slicing. *J. Geophys. Res.*, **104**, 24 547–24 555.
- Gao, B.-C., P. Yang, W. Han, R. R. Li, and W. J. Wiscombe, 2002: An algorithm using visible and 1.375 mm channels to retrieve cirrus cloud reflectances from aircraft and satellite data. *IEEE Trans. Geosci. Remote Sens.*, **40**, 1659–1688.
- Garand, L., 2003: Toward an integrated land–ocean surface skin temperature analysis from the variational assimilation of infrared radiances. *J. Appl. Meteor.*, **42**, 570–583.
- Goerss, J. S., C. S. Velden, and J. D. Hawkins, 1998: The impact of multispectral GOES-8 wind information on Atlantic tropical cyclone track forecasts in 1995. Part II: NOGAPS forecasts. *Mon. Wea. Rev.*, **126**, 1219–1227.
- Gu, Y., W. I. Rose, and G. J. S. Bluth, 2003: Retrieval of mass and sizes of particles in sandstorms using two MODIS IR bands: A case study of April 7, 2001 sandstorm in China. *Geophys. Res. Lett.*, **30**, 1805, doi:10.1029/2003GL017405.
- Gurka, J. J., and G. J. Dittberner, 2001: The next generation GOES instruments: Status and potential impact. Preprints, *Fifth Symp. on Integrated Observing Systems*, Albuquerque, NM, Amer. Meteor. Soc., CD-ROM, 7.9.
- Hannon, S., L. L. Strow, and W. W. McMillan, 1996: Optical spectroscopic techniques and instrumentation for atmospheric and space research II. *Proc. SPIE*, **2830**, 94–105.
- Hayden, C. M., 1996: Meteorological features from principal component image transformation of GOES imagery. *Proc. GOES-8 and Beyond*, Denver, CO, International Society of Optical Engineering, 111–121.
- , and J. Clark, 2002: Principal component image analysis of MODIS for volcanic ash. Part II: Simulation of current GOES and GOES-M imagers. *J. Appl. Meteor.*, **41**, 1003–1010.
- , G. S. Wade, and T. J. Schmit, 1996: Derived product imagery from GOES-8. *J. Appl. Meteor.*, **35**, 153–162.
- , T. J. Schmit, and J. M. Daniels, 2003: Imager and sounder radiance and product validations for the GOES-12 science test. NOAA Tech. Rep. 115, U.S. Department of Commerce, Washington, DC, 70 pp.
- Hutchison, K. D., 1999: Application of AVHRR-3 imagery for improved detection of thin cirrus clouds and specification of cloud-top phase. *J. Atmos. Oceanic Technol.*, **16**, 1885–1899.
- Karnieli, A., Y. J. Kaufman, L. A. Remer, and A. Wald, 2001: AFRI—Aerosol free vegetation index. *Remote Sens. Environ.*, **77**, 10–21.
- Kaufman, Y. J., A. E. Wald, L. A. Remer, B.-C. Gao, R.-R. Li, and L. Flynn, 1997: The MODIS 2.1 μm channel—Correlation with visible reflectance for use in remote sensing of aerosol. *IEEE Trans. Geosci. Remote Sens.*, **35**, 1286–1298.
- Kim, D., and S. G. Benjamin, 2000: Assimilation of cloud-top pressure derived from GOES sounder data into MAPS/RUC. Preprints, *10th Conf. on Satellite Meteorology and Oceanography*, Long Beach, CA, Amer. Meteor. Soc., 110–113.
- King, M. D., Y. J. Kaufman, W. P. Menzel, and D. Tanre, 1992: Remote sensing of cloud, aerosol and water vapor properties from the Moderate Resolution Imaging Spectrometer (MODIS). *IEEE Trans. Geosci. Remote Sens.*, **30**, 2–27.
- , and Coauthors, 2003: Cloud and aerosol properties, precipitable water, and profiles of temperature and water vapor from MODIS. *IEEE Trans. Geosci. Remote Sens.*, **41**, 442–458.
- Kittaka, C., and Coauthors, 2004: Utilizing MODIS satellite observations to monitor and analyze fine particulate matter, PM2.5, transport event. Preprints, *Sixth Conf. on Atmospheric Chemistry: Air Quality in Megacities*, Seattle, WA, Amer. Meteor. Soc., CD-ROM, 1.3.
- Kogan, F. N., 1990: Remote sensing of weather impacts on vegetation in non-homogeneous areas. *Int. J. Remote Sens.*, **11**, 1405–1419.
- Kossin, J. P., 2002: Daily hurricane variability inferred from GOES infrared imagery. *Mon. Wea. Rev.*, **130**, 2260–2270.
- Lee, T. F., F. J. Turk, and K. Richardson, 1997: Stratus and fog products using GOES-8–9 3.9- μm data. *Wea. Forecasting*, **12**, 664–677.
- Legeckis, R., C. W. Brown, and P. S. Chang, 2002: Geostationary satellites reveal motions of ocean surface fronts. *J. Mar. Syst.*, **37**, 3–15.

- Li, J., C. C. Schmidt, J. P. Nelson III, T. J. Schmit, and W. P. Menzel, 2001: Estimation of total atmospheric ozone from GOES sounder radiances with high temporal resolution. *J. Atmos. Oceanic Technol.*, **18**, 157–168.
- , T. J. Schmit, and W. P. Menzel, 2002: Advanced Baseline Sounder (ABS) for future Geostationary Operational Environmental Satellites (GOES-R and beyond). *Proc. SPIE*, **4895**, 103–110.
- , W. P. Menzel, Z. Yang, R. A. Frey, and S. A. Ackerman, 2003: High-spectral resolution surface and cloud type classification from MODIS multi-spectral band measurements. *J. Appl. Meteor.*, **42**, 204–226.
- , —, F. Sun, T. J. Schmit, and J. Gurka, 2004a: AIRS sub-pixel cloud characterization using MODIS cloud products. *J. Appl. Meteor.*, **43**, 1083–1094.
- , —, W. Zhang, F. Sun, T. J. Schmit, J. Gurka, and E. Weisz, 2004b: Synergistic use of MODIS and AIRS in a variational retrieval of cloud parameters. *J. Appl. Meteor.*, **43**, 1619–1634.
- McCann, D. W., 1983: The enhanced-V: A satellite observable severe storm signature. *Mon. Wea. Rev.*, **111**, 887–894.
- Menzel, W. P., and J. F. W. Purdom, 1994: Introducing GOES-I: The first of a new generation of geostationary operational environmental satellites. *Bull. Amer. Meteor. Soc.*, **75**, 757–781.
- Moeller, C. C., S. A. Ackerman, K. I. Strabala, W. P. Menzel, and W. L. Smith, 1996: Negative 11 micron minus 12 micron brightness temperature differences: A second look. Preprints, *Eighth Conf. on Satellite Meteorology and Oceanography*, Atlanta, GA, Amer. Meteor. Soc., 313–316.
- Moody, J. L., A. J. Wimmers, and J. C. Davenport, 1999: Remotely sensed specific humidity: Development of a derived product from the GOES Imager channel 3. *Geophys. Res. Lett.*, **26**, 59–62.
- Mosher, F. R., 2001: A satellite diagnostic of global convection. Preprints, *11th Conf. on Satellite Meteorology and Oceanography*, Madison, WI, Amer. Meteor. Soc., CD-ROM, P3.58.
- Nieman, S. J., J. Schmetz, and W. P. Menzel, 1993: A comparison of several techniques to assign heights to cloud tracers. *J. Appl. Meteor.*, **32**, 1559–1568.
- NOAA/NESDIS, 2001: Second GOES Users Conference, Conf. Rep., U.S. Dept. of Commerce, Boulder, CO, 45 pp. [Available online at http://www.osd.noaa.gov/goes_R/goesrconf.htm.]
- Platnick, S., M. D. King, S. A. Ackerman, W. P. Menzel, B. A. Baum, J. C. Riedi, and R. A. Frey, 2003: The MODIS cloud products: Algorithms and examples from Terra. *IEEE Trans. Geosci. Remote Sens.*, **41**, 459–473.
- Prata, A. J., 1989: Observations of volcanic ash clouds in the 10–12 mm window using AVHRR/2 data. *Int. J. Remote Sens.*, **10**, 751–761.
- Prins, E. M., J. M. Feltz, W. P. Menzel, and D. E. Ward, 1998: An overview of GOES-8 diurnal fire and smoke results for SCAR-B and 1995 fire season in South America. *J. Geophys. Res.*, **103**, 31 821–31 835.
- Purdom, J. F. W., 1976: Some uses of high-resolution GOES imagery in the mesoscale forecasting of convection and its behavior. *Mon. Wea. Rev.*, **104**, 1474–1483.
- Raymond, W. H., G. S. Wade, and T. H. Zapotocny, 2004: Assimilating GOES brightness temperatures. Part I: Upper-tropospheric moisture. *J. Appl. Meteor.*, **43**, 17–27.
- Realmuto, V. J., A. J. Sutton, and T. Elias, 1997: Multi-spectral thermal infrared mapping of sulfur dioxide plumes: A case study from the East Rift Zone of Kilauea Volcano, Hawaii. *J. Geophys. Res.*, **102**, 15 057–15 072.
- Roberts, R. D., and S. Rugledge, 2003: Nowcasting storm initiation and growth using GOES-8 and WSR-88D data. *Wea. Forecasting*, **18**, 562–584.
- Schmetz, J., H. Woick, S. Tjemkes, and J. Rattenborg, 1998: From Meteosat to Meteosat Second Generation. Preprints, *Ninth Conf. on Satellite Meteorology and Oceanography*, Paris, France, Amer. Meteor. Soc., 335–338.
- , P. Pili, S. Tjemkes, D. Just, J. Kerkmann, S. Rota, and A. Ratier, 2002: An introduction to Meteosat Second Generation (MSG). *Bull. Amer. Meteor. Soc.*, **83**, 977–992.
- Schmidt, C., J. Li, and F. Sun, 2004: Simulation of and comparison between GIFTS, ABI, and GOES I-M sounder ozone estimates and applications to HES. Preprints, *20th Int. Conf. on Interactive Information Processing Systems (IIPS) for Meteorology, Oceanography, and Hydrology*, Seattle, WA, Amer. Meteor. Soc., CD-ROM, P2.37.
- Schmit, T. J., E. M. Prins, A. J. Schreiner, and J. J. Gurka, 2001: Introducing the GOES-M imager. *Natl. Wea. Assoc. Digest*, **25**, 28–37.
- , W. F. Feltz, W. P. Menzel, J. Jung, A. P. Noel, J. N. Heil, J. P. Nelson III, and G. S. Wade, 2002: Validation and use of GOES sounder moisture information. *Wea. Forecasting*, **17**, 139–154.
- Schreiner, A. J., and T. J. Schmit, 2001: Derived cloud products from the GOES-M Imager. Preprints, *11th Conf. on Satellite Meteorology and Oceanography*, Madison, WI, Amer. Meteor. Soc., CD-ROM, P3.60.
- , D. A. Unger, W. P. Menzel, G. P. Ellrod, K. I. Strabala, and J. L. Pellett, 1993: A comparison of

- ground and satellite observations of cloud cover. *Bull. Amer. Meteor. Soc.*, **74**, 1851–1861.
- , T. J. Schmit, and W. P. Menzel, 2001: Trends and observations of clouds based on GOES sounder data. *J. Geophys. Res.*, **106**, 20 349–20 363.
- Scofield, R. A., and R. J. Kuligowski, 2003: Status and outlook of operational satellite precipitation algorithms for extreme precipitation events. *Wea. Forecasting*, **18**, 1037–1051.
- Seki, M. P., J. J. Polovina, R. E. Brainard, R. R. Bidgare, C. L. Leonard, and D. G. Foley, 2001: Biological enhancement at cyclonic eddies tracked with GOES thermal imagery in Hawaiian waters. *Geophys. Res. Lett.*, **28**, 1583–1586.
- Sieglaff, J. M., and T. J. Schmit, 2003: Vegetation monitoring and thin cirrus detection on the next generation GOES imager. Preprints, *12th Conf. on Satellite Meteorology and Oceanography*, Long Beach, CA, Amer. Meteor. Soc., CD-ROM, P5.4.
- Smith, W. L., and Coauthors, 1999: NAST-I: Results from revolutionary aircraft sounding spectrometer. *Proc. SPIE*, **3756**, 2–8.
- Soden, B. J., and F. P. Bretherton, 1993: Upper tropospheric relative humidity from the GOES 6.7 mm channel: Method and climatology for July 1987. *J. Geophys. Res.*, **98**, 16 669–16 688.
- Steinbrecht, W., H. Claude, U. Köhler, and K. P. Hoinka, 1998: Correlations between tropopause height and total ozone: Implications for long-term changes. *J. Geophys. Res.*, **103**, 19 183–19 192.
- Strabala, K. I., S. A. Ackerman, and W. P. Menzel, 1994: Cloud properties inferred from 8–12-mm data. *J. Appl. Meteor.*, **33**, 212–229.
- Suomi, V. E., and R. Parent, 1968: A color view of planet earth. *Bull. Amer. Meteor. Soc.*, **49**, 74–75.
- Szyndel, M., J.-N. Thepaut, and G. Kelly, 2003: Developments in the assimilation of geostationary radiances at ECMWF/EUMETSAT/ECMWF Fellowship Programme, First Year Report, 25 pp.
- Tarpley, J. D., S. R. Schnieder, and R. L. Money, 1984: Global vegetation indices from NOAA-7 meteorological satellite. *J. Climate Appl. Meteor.*, **23**, 4491–4503.
- Vane, G., 1987: Airborne Visible/Infrared Imaging Spectrometer (AVIRIS). JPL Publication 87-38, Jet Propulsion Lab, Pasadena, CA.
- Velden, C. S., C. M. Hayden, S. J. Nieman, W. P. Menzel, S. Wanzong, and J. S. Goerss, 1997: Upper-tropospheric winds derived from geostationary satellite water vapor observations. *Bull. Amer. Meteor. Soc.*, **78**, 173–173.
- , T. L. Olander, and R. M. Zehr, 1998a: Development of an objective scheme to estimate tropical cyclone intensity from digital geostationary satellite infrared imagery. *Wea. Forecasting*, **13**, 172–186.
- , —, and S. Wanzong, 1998b: The impact of multi-spectral GOES-8 wind information on Atlantic tropical cyclone track forecasts in 1995. Part I: Dataset methodology, description, and case analysis. *Mon. Wea. Rev.*, **126**, 1202–1218.
- Vicente, G. A., R. A. Scofield, and W. P. Menzel, 1998: The operational GOES infrared rainfall estimation technique. *Bull. Amer. Meteor. Soc.*, **79**, 1883–1898.
- Walker, N., S. Myint, A. Babin, and A. Haag, 2003: Advances in satellite radiometry for the surveillance of surface temperatures, ocean eddies and upwelling processes in the Gulf of Mexico using GOES-8 measurements during summer. *Geophys. Res. Lett.*, **30**, 1854, doi:10.1029/2003GL017555.
- Weldon, R. B., and S. J. Holmes, 1991: Water vapor imagery—Interpretation and applications to weather analysis and forecasting. NOAA Tech. Rep. NESDIS 57, 213 pp.
- Woick, H., J. Schmetz, and S. Tjemkes, 1997: An introduction to Meteosat Second Generation imagery and products. *Proc. 1997 Meteorological Data Users' Conf.*, Brussels, Belgium, EUMETSAT, 395–400.
- Wu, X., W. P. Menzel, and G. S. Wade, 1999: Estimation of sea surface temperatures using GOES-8/9 radiance measurements. *Bull. Amer. Meteor. Soc.*, **80**, 1127–1138.
- Wylie, D. P., and P. H. Wang, 1997: Comparison of cloud frequency data for the High Resolution Infrared Radiometer Sounder and the Stratospheric Aerosol and Gas Experiment II. *J. Geophys. Res.*, **102**, 29 893–29 900.
- , and W. P. Menzel, 1999: Eight years of high cloud statistics using HIRS. *J. Climate*, **12**, 170–184.
- , —, H. M. Woolf, and K. I. Strabala, 1994: Four years of global cirrus cloud statistics using HIRS. *J. Climate*, **7**, 1972–1986.